



Cite this: *Environ. Sci.: Nano*, 2017, 4, 1512

## Simulation of magnetite nanoparticle mobility in a heterogeneous flow cell†

Bonnie A. Lyon-Marion,<sup>a</sup> Matthew D. Becker,<sup>a</sup> Anthony A. Kmetz,<sup>‡a</sup> Edward Foster,<sup>b</sup> Keith P. Johnston,<sup>b</sup> Linda M. Abriola<sup>b</sup> and Kurt D. Pennell<sup>\*,b</sup>

Engineered nanomaterials have been proposed for a range of subsurface applications including groundwater remediation, treatment of contaminated soils, and characterization of flow. The ability to accurately predict nanoparticle (NP) mobility in the environment is critical for assessing NP performance and designing subsurface applications. The objective of this study was to evaluate the ability of a numerical simulator that accounts for the influence of varying electrolyte and NP concentrations to predict experimental observations of polymer-coated magnetite nanoparticle (nMag) transport and retention in a heterogeneous, multi-dimensional flow cell (0.64 m length × 0.38 m height × 1.4 cm internal thickness, referred to as “2.5-dimensional” or “2.5D” due to the internal thickness width). A series of column experiments was performed to independently determine model input parameters, including the maximum NP retention capacity and attachment rate. Localized injection of nMag into the heterogeneous flow cell demonstrated preferential flow around a lower permeability lens and the downward migration of higher density nMag suspensions. Numerical simulations successfully captured the observed flow path of the nMag pulse injections, and provided close fits to spatially distributed aqueous and solid-phase nMag measurements obtained within the heterogeneous flow field. Experimental and modeling results demonstrated that relatively small contrasts in fluid density (e.g., 0.01 g mL<sup>-1</sup>) can result in flow instabilities and downward migration of nMag. This work provides the first direct comparison between model simulations and experimental observations of NP transport and retention in a 2.5D heterogeneous flow domain and demonstrates the importance of accounting for relevant physical and chemical properties in order to accurately describe NP fate and transport.

Received 14th February 2017,  
Accepted 19th May 2017

DOI: 10.1039/c7en00152e

rsc.li/es-nano

### Environmental significance

The ability to accurately predict nanoparticle transport and retention in porous media under environmentally relevant conditions is critical for the design and assessment of potential field-scale environmental applications of engineered nanomaterials. This work provides the first direct comparison of parameterized model predictions to experimental measurements of spatially distributed nanoparticle transport and retention in a heterogeneous, multi-dimensional domain. Results demonstrated that small fluid density contrasts (e.g., 0.01 g mL<sup>-1</sup>) can play an important role in nanoparticle mobility in heterogeneous porous media, and therefore, should be accounted for when attempting to simulate nanoparticle transport in subsurface environments. While this study focused on magnetite nanoparticles, the nanoparticle transport model can be applied to a range of conditions, including nanoparticle delivery scenarios in salinity-impacted aquifer formations.

## Introduction

Engineered nanomaterials have shown promise for a range of environmental applications, including remediation of

groundwater contaminants,<sup>1–4</sup> removal of heavy metals from water,<sup>5</sup> and treatment of contaminated soils.<sup>6</sup> Additionally, the use of nanoparticles (NPs) as contrast agents has been proposed for subsurface characterization of oilfield

<sup>a</sup> Department of Civil and Environmental Engineering, Tufts University, 200 College Avenue, Medford, Massachusetts 02155, USA.

E-mail: kurt.pennell@tufts.edu; Fax: +617 627 3994; Tel: +617 627 3099

<sup>b</sup> McKetta Department of Chemical Engineering, The University of Texas at Austin, Austin, Texas 78712, USA

† Electronic supplementary information (ESI) available. Nanoparticle synthesis schematic, TEM image, and additional details on analytical methods and mathe-

matical model development; figures showing 1D column transport of nMag, fitted  $S_{max}$  relationship with normalized mass flux, observed/simulated non-reactive tracer transport, observed and simulated nMag transport and BTCs for control injection, effect of density on simulated nMag transport, SEM images; and table showing nMag injection parameters for flow cell. See DOI: 10.1039/c7en00152e

‡ Current affiliation: Aramco Services Company: Aramco Research Center – Boston, Cambridge, MA 02139, USA.

reservoirs,<sup>7–9</sup> a technique that could also be applied to characterize flow in heterogeneous aquifer formations. Each of these potential applications relies on the delivery of aqueous solutions of engineered NPs to a targeted subsurface location or region, whether the objective is to treat a contaminated aquifer (e.g., nanoscale zero-valent iron, nZVI),<sup>3</sup> to interact with oil/water interfaces,<sup>4</sup> or to function as contrast agents for subsurface characterization<sup>7–9</sup> (e.g., superparamagnetic iron oxide NPs). Thus, the ability to accurately predict NP transport and retention in porous media under environmentally relevant conditions is critical for the design and assessment of field-scale nanoparticle technologies.

Nanoparticle mobility in porous media is governed by NP–NP and NP–surface interactions, which are impacted by solution chemistry (e.g., ionic strength, pH, co-constituents)<sup>10</sup> as well as solid phase surface properties.<sup>11,12</sup> In general, increasing ionic strength results in greater NP aggregation and deposition, as a result of electrical double layer suppression and decreased electrostatic repulsion between NPs and solid surfaces.<sup>13</sup> This type of attachment behavior has been observed for many types of NPs including iron,<sup>14</sup> metal oxides,<sup>15,16</sup> carbon-based,<sup>17,18</sup> silver,<sup>19</sup> titanium dioxide,<sup>20</sup> and quantum dots.<sup>21</sup> However, recent advances in surface coating techniques now enable stabilized NP suspensions at high ionic strength, IS (e.g., IS > 1 M), and greatly reduced NP attachment even in fine-grained porous media (e.g., crushed sandstone).<sup>22–24</sup> The subsurface environment encountered by NP introduces additional complexity, including heterogeneity resulting from layers or lenses of lower permeability and transient ionic strength conditions that can lead to altered flow and transport behavior.<sup>25</sup> Phenrat *et al.* evaluated the transport of olefin-maleic acid copolymer-modified nZVI in a two-dimensional flow cell containing layers of fine, medium, and coarse sand ( $d_{50} = 99, 330, \text{ and } 880 \mu\text{m}$ , respectively) with a background electrolyte of 1 mM NaHCO<sub>3</sub>.<sup>12</sup> The authors observed preferential flow of nZVI into regions of higher permeability media and deposition in regions of low velocity (low fluid shear), demonstrating the influence of porous media heterogeneity on NP transport.

Mathematical models used to predict NP mobility in porous media are often based on modifications of clean-bed colloid filtration theory (CFT),<sup>26</sup> in which colloid transport and deposition are governed by the advection–dispersion reaction (ADR) equation with a first order decay reaction rate to describe the attachment of colloidal particles to porous media. Tufenkji and Elimelech demonstrated that while CFT may be valid for highly idealized deposition conditions (i.e., glass bead porous media and spherical latex microparticles), physicochemical non-idealities, which would be experienced in any natural system, can contribute to significant deviations from CFT.<sup>27</sup> Li *et al.* (2008) proposed the inclusion of a maximum retention capacity term ( $S_{\text{max}}$ ), which was shown to more accurately model the transport and deposition of nC<sub>60</sub> in glass beads and washed Ottawa sand compared to traditional CFT.<sup>28,29</sup> Another process that is often considered

in NP transport modeling in porous media is physical particle filtration, or straining, which accounts for the entrapment of particles in pore throats. For colloid transport, straining is often considered to be significant when the ratio of particle diameter ( $d_p$ ) to mean grain diameter ( $d_g$  or  $d_{50}$ ) is greater than 0.0017, 0.002, or 0.008.<sup>30–32</sup> More recent work has demonstrated straining of polymer-coated nZVI at even lower  $d_p/d_{50}$  ratios of  $2.24 \times 10^{-4}$ – $1.23 \times 10^{-3}$  and iron oxide NPs at  $d_p/d_{50}$  ratios of  $5.5 \times 10^{-5}$ – $1.8 \times 10^{-4}$ .<sup>33,34</sup> The authors of these studies hypothesized that the observed straining at ratios lower than previously reported values<sup>32</sup> may have resulted from the formation of nanoparticle aggregates (400–550 nm) that enhanced the extent of straining.

A number of studies have employed numerical simulators, based on the concepts discussed above, to successfully reproduce experimental observations of NP transport and retention in porous media.<sup>28,29,35–38</sup> However, the majority of these investigations have focused on the fitting of data from one-dimensional column transport experiments performed under idealized conditions (e.g., employing homogeneous packing of glass beads or acid-washed sands, high pore-water velocities, and uniform solution composition). More recent mathematical modeling studies have also considered NP mobility under transient ionic strength conditions.<sup>19,39–41</sup> For example, Becker and colleagues modified an existing variable density groundwater flow simulator to incorporate the coupled effects of transient ionic strength on iron oxide NP transport, deposition, and release in a homogeneously packed column.<sup>39</sup> In their study, the numerical simulator was able to accurately reproduce experimental observations of attached NP release and breakthrough following delivery of distilled, deionized water (IS  $\approx$  0.0 M).

While useful for assessing the impacts of individual experimental parameters on NP transport, the column studies highlighted above are not representative of conditions expected for the field application of NP technologies in natural subsurface environments (i.e., multi-dimensional, chemically and physically heterogeneous systems). Thus, a significant gap in much of the existing NP mobility literature is the upscaling of batch and column studies to multi-dimensional, heterogeneous flow domains and the associated parameterization and validation of mathematical models for the accurate prediction of NP transport behavior at larger scales (i.e., >1 m). To date, the few published studies of NP transport at larger scales have generally failed to couple modeling and experiments, focusing either on data collection/experimental observation or on hypothetical modeling scenarios. A limited number modeling studies have investigated the mobility of NPs at larger scales through application of models parameterized with the results of laboratory column experiments.<sup>42–44</sup> In those studies, using mathematical models based on CFT,<sup>28</sup> hypothetical scenarios of fullerene NP transport were explored in meter-scale homogeneous and heterogeneous domains subject to various boundary conditions. Other published work

has investigated nZVI transport in two-dimensional flow cells (0.3–0.7 m length)<sup>12,45</sup> and larger field-scale tests (3–10 m length),<sup>46,47</sup> but did not incorporate mathematical modeling work. In one study that did couple experimental observations with mathematical modeling, Kanel and colleagues<sup>48</sup> evaluated two-dimensional transport of nZVI in a homogeneous flow cell packed with glass beads and were able to accurately simulate the NP plume path using SEAWAT, a numerical simulator developed by the United States Geological Survey.<sup>49</sup> Two more recent studies applied 2D and 3D mathematical modeling to experimental observations of nZVI transport in laboratory<sup>50</sup> and field-scale systems<sup>51</sup> and found good agreement between model fits and experimental data. While the previous work highlighted above provides useful insight into the behavior of NPs in multi-dimensional domains, NP transport models have not yet been validated through quantitative comparison of simulations to spatially distributed transport and retention data collected in larger-scale, multi-dimensional, heterogeneous experimental systems (*i.e.*, through comparisons of model predictions, based upon independently measured parameters, to experimental observations, rather than through model fitting to experimental data).

The objective of this study was to evaluate the performance of a laboratory-parameterized, multi-dimensional NP transport model by comparing model simulations with experimental measurements of NP transport and retention in a heterogeneous flow cell (0.64 m length  $\times$  0.38 m height  $\times$  1.4 cm internal thickness, which will be referred to as “2.5-dimensional” or “2.5D,” because of the internal thickness width). The heterogeneity evaluated in this study refers to spatial variations in porous media grain size, leading to heterogeneous flow fields and spatial and temporal variations in attachment properties. The multi-dimensional NP transport model employed here is based on SEAWAT (ver. 4) code,<sup>49</sup> originally developed to model seawater intrusion in coastal formations. This simulator, which accounts for variable aqueous phase density and viscosity, was modified to describe NP transport subject to a limiting attachment capacity ( $S_{\max}$ ) implemented through a site-blocking function,  $\psi_i$ ,<sup>28,29</sup> as previously described.<sup>39</sup> Polymer-coated magnetite NPs (nMag) were selected for the flow cell experiment due to their stability at high salinity (no aggregation after 1 month at 90 °C in brine solution, 8 wt% NaCl + 2 wt% CaCl<sub>2</sub>)<sup>22</sup> and relatively low propensity for attachment to porous media (*e.g.*, crushed sandstone with 5% clay content) demonstrated in previous work.<sup>22–24</sup> An initial set of column studies was performed to independently assess nMag mobility and to obtain model input parameters for each porous medium. nMag suspensions (*ca.* 2500 mg L<sup>-1</sup> as Fe<sub>3</sub>O<sub>4</sub>) were introduced through injection well side ports into a flow cell containing lenses of lower permeability porous medium. Aqueous phase side-port (internal) and effluent samples, as well as solid concentration data (collected at the conclusion of the experiment), were compared to numerical simulations to assess model performance.

## Experimental materials and methods

### Nanoparticles

Magnetite NPs were synthesized using the procedure described by Ureña-Benavides *et al.*<sup>24</sup> Citrate-stabilized NP clusters were first coated with tetraethyl orthosilicate (TEOS) (Sigma-Aldrich, St. Louis, MO) to improve surface reactivity<sup>52</sup> prior to amine-functionalization with 3-aminopropyl triethoxysilane (APTES) (Sigma-Aldrich, St. Louis, MO). Following TEOS-coating, nMag was separated magnetically and rinsed twice with deionized (DI) water. Poly(2-acrylamido-2-methylpropanesulfonate-*co*-acrylic acid), or poly(AMPS-*co*-AA), which was synthesized from potassium persulfate (Acros Organics, Geel, Belgium), sodium metabisulfite (Alfa Aesar, Ward Hill, MA), 2-acrylamido-2-methyl-1-propanesulfonic acid (Sigma-Aldrich, St. Louis, MO), and acrylic acid (Alfa Aesar, Ward Hill, MA), was then grafted onto the NPs at an AMPS:AA ratio of 3:1. To remove excess polymer after the AMPS:AA-grafting step, the NPs were centrifuged three times (10 minutes at 11 000 rpm) and redispersed. The organic content of the polymer-coated nMag was  $37 \pm 5$  wt%, measured using a Mettler-Toledo (Columbus, OH) SDTA851e thermogravimetric analyzer (TGA). Magnetic susceptibility measurements were performed to confirm the type of iron oxide in the synthesized NPs (*i.e.*, Fe<sub>3</sub>O<sub>4</sub>, magnetite, rather than Fe<sub>2</sub>O<sub>3</sub>, hematite). The zeta potential of the final polymer-coated nMag was  $-47 \pm 1$  mV. Within the 30 minutes prior to injection, the nMag stock suspension was bath-sonicated for 5 minutes, diluted to achieve a concentration of 2500 mg L<sup>-1</sup> (as Fe<sub>3</sub>O<sub>4</sub>) in brine (8 wt% NaCl, 2 wt% CaCl<sub>2</sub>) prepared in degassed DI water, and adjusted to pH 7 using 1 M NaOH. The brine background solution was chosen to simulate the high salinity that would be encountered in deep subsurface reservoirs for the application of NPs as contrast agents.<sup>23</sup> A schematic of the synthesis process and transmission electron microscopy (TEM) image of the polymer-coated nMag are included in the ESI† Fig. S1 and S2.

### Porous media

The 40–50 mesh and 80–100 mesh-size fractions of quartz silica sand were obtained by sieving 2-lb. increments of F-50 Ottawa Sand (U.S. Silica, Berkeley Springs, WV) for 10 minute cycles with an RX-29 Ro-Tap sieve shaker (W.S. Tyler Inc., Mentor, OH) until  $\geq 95\%$  weight was retained on the desired mesh screen. These fractions will herein be referred to as coarse (40–50 mesh) and fine (80–100 mesh) sand. The fine sand fraction was washed to remove metal oxide impurities<sup>53</sup> by soaking in 1 M HNO<sub>3</sub>, rinsed with DI water, and placed in an ultrasonic bath containing 0.007 M Na<sub>2</sub>HPO<sub>4</sub> for at least 10 h, followed by rinsing with DI water until pH 7 was reached and then oven-dried at 200 °C for 12 h. The  $d_{50}$  values of coarse and fine Ottawa sand were 335  $\mu\text{m}$  and 165  $\mu\text{m}$ , respectively. The permeabilities of wet-packed coarse and fine sand were determined to be 48.8 Darcy (D) ( $4.81 \times 10^{-11} \text{ m}^2$ ) and 4.3 D ( $4.27 \times 10^{-12} \text{ m}^2$ ), respectively, based on a constant head permeameter test conducted in accordance

with the American Society for Testing and Materials (ASTM) Method D2434-68.<sup>54</sup>

### Column experiments

The experimental apparatus used for the column studies consisted of a syringe pump (Harvard Apparatus, Inc., Holliston, MA), a borosilicate glass column (10 cm length  $\times$  2.5 cm inner diameter, Kontes, Vineland, NJ) equipped with PTFE end plates fitted with a 40-mesh nylon screen and 70  $\mu\text{m}$  filter to retain the sand and distribute injected fluids, and a fraction collector (Spectrum Chromatography, Houston, TX). For each experiment, columns were dry-packed in 1 cm increments with either coarse or fine sand, which yielded porosity values of 0.37 and 0.38, respectively. After packing, the columns were purged with  $\text{CO}_2$  gas for 20 minutes and then saturated with 10 pore volumes (PVs) of brine (8 wt% NaCl, 2 wt%  $\text{CaCl}_2$ ) in degassed DI water in the upflow direction using an ISO-100 Isocratic Pump (Chrom Tech, Apple Valley, MN). The  $\text{CO}_2$  purging step was performed to replace ambient air with  $\text{CO}_2$ , which readily dissolved during the initial saturation process, ensuring that residual gas did not exist in soil pores. To characterize water flow and hydrodynamic dispersion in each column, non-reactive tracer tests were carried out by injecting 3.5 PVs of 2 M NaBr (equivalent to IS of the brine solution), followed by 3.5 PVs of brine. After the tracer test, a 3.5 PV pulse of nMag (nominal concentration of 2500  $\text{mg L}^{-1}$ ) in brine was injected in the upflow direction, followed by 3.5 PVs of brine. To obtain model parameters as a function of flow rate, the fine sand column was run at two different flow rates (0.26  $\text{mL min}^{-1}$  or 1.78  $\text{mL min}^{-1}$ ), which correspond to seepage velocities of 2 m per day and 12 m per day, respectively. Due to the relatively high mobility of nMag in the coarse sand at 2 m per day (97% mass breakthrough), only the slow flow rate was used to parameterize the model for the coarse sand (Table 1).

### Heterogeneous flow cell

A 2.5D flow cell (0.64 m length  $\times$  0.38 m height  $\times$  1.4 cm internal thickness) was constructed from two pieces of glass separated by a stainless steel frame. The flow cell was packed under water-saturated conditions with the coarse sand as the background medium and a lens (approx. 3.5 cm height  $\times$  12.5 cm length) of the fine sand to evaluate nMag mobility

under heterogeneous conditions. End chambers (1.27 cm  $\times$  1.27 cm) were screened over the height of the flow cell. Influent and effluent wells were constructed from 0.64 cm outer diameter stainless steel tubing that was inserted into the screened end chambers. A schematic diagram of the packed flow cell, which had a PV of approximately 1.4 L, is shown in Fig. 1. The top half of the flow cell was used for preliminary experiments that are not discussed here. Injection and sampling side-ports were comprised of borosilicate glass tubes with PTFE-lined septa that were glued into ports in the front glass panel using RTV silicone glue (Dow Corning Corporation, Auburn, MI). At each injection port, stainless steel screens were placed inside the flow cell to promote uniform flow into the media. A constant head reservoir was used to deliver background electrolyte solutions through the flow cell at a pore-water velocity of approximately 2 m per day, which is representative of the upper limit of reservoir pore-water velocities under natural gradient conditions.<sup>55</sup> The flow cell was initially saturated with 2 mM  $\text{CaCl}_2$  + 0.05 mM  $\text{NaHCO}_3$  and non-reactive tracer tests (3.05 mM NaBr + 5  $\text{mg L}^{-1}$  fluorescein) were carried out through the influent end chamber and sequentially through each injection port. Following the non-reactive tracer tests, the background electrolyte was switched to brine (8 wt% NaCl + 2 wt%  $\text{CaCl}_2$ ) in incremental steps (2.5 PVs each of 25%, 50%, 75%, and 100% brine) to ensure complete saturation of the domain. Two NP injection experiments were performed separately through injection ports A4 and D4, which were located adjacent to the fine sand lens and the coarse sand background control (no lens), respectively. For each experiment, 200 mL of an nMag suspension in brine (nominal concentration of 2500  $\text{mg L}^{-1}$  as  $\text{Fe}_3\text{O}_4$ ) was injected using a peristaltic pump at 0.75  $\text{mL min}^{-1}$ , with head-driven background flow of brine at 2 m per day. Samples (0.25 mL) were collected from downstream sampling ports every 20 minutes during and after the nMag injection at a rate of approximately 0.5  $\text{mL min}^{-1}$ , until the mobile nMag pulse passed through the effluent chamber. The total volume of samples collected from downstream ports was 19.75 mL for the A4 injection and 20 mL for the D4 injection, which represented 1.2% and 1.7%, respectively, of the total aqueous solution (background flow + injected nanoparticle suspension) over the course of each experiment. The sampling procedure was therefore assumed to have negligible impact on the overall flow field. Details of the injection

**Table 1** Column conditions, fitted model parameters ( $k_{\text{att}}$  and  $S_{\text{max}}$ ), and associated empirical parameters for nMag transport under varying flow rates and porous media types

Porous Media <sup>a</sup>	Permeability ( $\text{m}^2$ )	Grain size, $d_c^b$ (m)	nMag conc. ( $\text{mg L}^{-1}$ )	nMag diameter <sup>c</sup> (nm)	$v_p$ (m per day)	nMag mass breakthrough (%)	$k_{\text{att}}^d$ ( $\text{h}^{-1}$ )	$\eta^e$ (unitless)	$\eta_o^f$ (unitless)	$\alpha^g$ (unitless)	$S_{\text{max}}^h$ ( $\mu\text{g g}^{-1}$ )
Coarse sand	$4.81 \times 10^{-11}$	$3.35 \times 10^{-4}$	2529	$202 \pm 4.2$	2	96.6	1.11	$5.12 \times 10^{-3}$	0.119	$4.30 \times 10^{-2}$	67
Fine sand	$4.27 \times 10^{-12}$	$1.65 \times 10^{-4}$	2890	$193 \pm 6.0$	2	91.8	1.56	$3.33 \times 10^{-3}$	0.192	$1.74 \times 10^{-2}$	124
Fine sand	$4.27 \times 10^{-12}$	$1.65 \times 10^{-4}$	2366	$209 \pm 3.4$	12	89.9	19.37	$6.11 \times 10^{-3}$	0.0462	$1.32 \times 10^{-1}$	106

<sup>a</sup> Coarse sand = 40–50 mesh Ottawa sand, fine sand = 80–100 mesh Ottawa sand. <sup>b</sup> Mean grain size. <sup>c</sup> Z-Average size measured by DLS, value represents average between triplicate samples at start and end of injection  $\pm$  standard deviation ( $n = 6$ ). <sup>d</sup> Fitted first order attachment rate, eqn (7). <sup>e</sup> Collector efficiency. <sup>f</sup> Single collector efficiency, eqn (8). <sup>g</sup> Attachment efficiency. <sup>h</sup> Retention capacity, equation (S1).

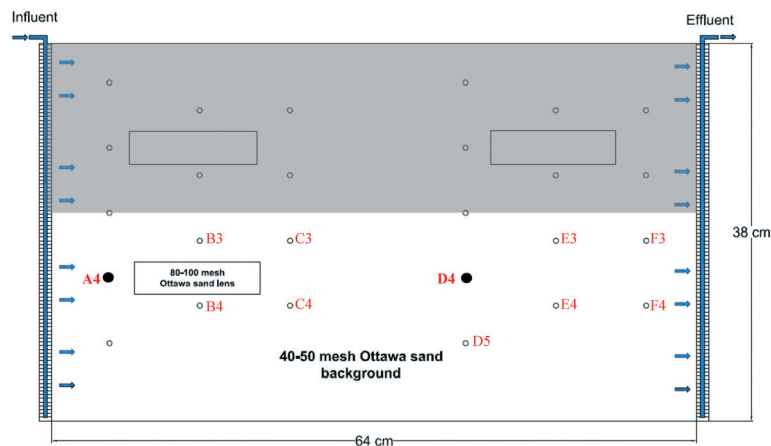


Fig. 1 Schematic of 2.5D flow cell. Injection ports are shown as filled circles and sampling ports are represented as open circles. For this study, two experiments were performed from injection ports A4 and D4 (top half of flow cell was used for a separate experiment not included here). The entire flow cell domain was used in all simulations to appropriately model the experimental system flow field.

conditions are presented in ESI† Table S1. Upon completion of flow cell experiments, the cell was disassembled and sand samples were collected to quantify the distribution of retained nMag.

### Analytical methods

The nMag concentration in stock suspensions was determined using microwave-assisted digestion (CEM Corporation, Matthews, NC) in concentrated nitric acid, diluted 4× in DI water and analyzed for total iron using an Optima 7300 DV inductively coupled plasma – optical emission spectroscopy (ICP-OES, Perkin Elmer, Waltham, MA). nMag concentration in aqueous column effluent and flow cell samples was determined using a Shimadzu UV-1800 spectrometer, operated at a wavelength of 600 nm (Shimadzu Corporation, Kyoto, Japan). Accuracy of the UV method was confirmed through analysis of nine duplicate effluent samples using the acid-digestion and ICP-OES method described above. For the analysis of retained nMag, solid samples collected at the completion of the flow cell experiment were oven-dried at 90 °C, and approximately 1 g of sand from each segment was microwave-digested in concentrated nitric acid, diluted 4× in DI water, and analyzed by ICP-OES. The nMag hydrodynamic diameter was measured by dynamic light scattering (DLS) using a Zetasizer Nano ZS Analyzer (Malvern Instruments Ltd., Southborough, MA), operated in back-scattering mode at an angle of 173°. Additional analytical details are provided in the SI, including bromide tracer test, density measurement, scanning electron microscopy (SEM) sample preparation and analysis.

### Mathematical model development

The coupled influence of transient brine chemistry and high concentration NP suspensions within a subsurface environment creates the potential for non-uniform and variable density flow conditions. Thus, a variable density aqueous phase

flow equation<sup>49</sup> was employed herein, following Becker *et al.*:<sup>39</sup>

$$\nabla \cdot \left[ \rho \frac{\mu}{\mu_0} \mathbf{K}_0 \left( \nabla h + \frac{\rho - \rho_0}{\rho_0} \nabla z \right) \right] = \rho S_{s,0} \frac{\partial h_0}{\partial t} + \theta_w \frac{\partial \rho}{\partial C} \frac{\partial C}{\partial t} - \rho_s q_s' \quad (1)$$

where  $S_{s,0}$  is the specific storage coefficient of the porous medium [ $L^{-1}$ ],  $h_0$  is the potentiometric head of the reference fluid (DI water) [L],  $\mathbf{K}_0$  is the hydraulic conductivity tensor [ $L T^{-1}$ ],  $\rho$  is fluid density [ $M L^{-3}$ ],  $\mu$  is fluid viscosity [ $M T^{-1} L^{-1}$ ],  $\rho_0$  and  $\mu_0$  are a reference density and viscosity, respectively, at which fluid and aquifer properties are known,  $\theta_w$  is the volumetric water content [-],  $h$  is pressure head [L],  $z$  is elevation head [L],  $C$  is aqueous concentration [ $M L^{-3}$ ], and  $\rho_s q_s'$  is a volumetric flux source term [ $M L^{-3} T^{-1}$ ] with source fluid density  $\rho_s$ . To account for the influence of brine concentration on fluid density, the spatio-temporal brine concentration profile was resolved using a traditional component mass balance equation:

$$\frac{\partial(\theta_w C_i)}{\partial t} = \nabla \cdot (\theta_w \mathbf{D}_i \nabla C_i) - \nabla \cdot (\theta_w v_p C_i) + q_s C_{i,s} + \sum_n R_n^i \quad (2)$$

Here  $C_i$  is the aqueous concentration of constituent  $i$  [ $M L^{-3}$ ],  $\mathbf{D}_i$  is the hydrodynamic dispersion tensor for constituent  $i$  [ $L^2 T$ ],  $v_p$  is the pore-water velocity [ $L T^{-1}$ ],  $q_s$  is a volumetric flow rate per unit volume of aquifer representing sources and/or sinks which include constituent  $i$  [ $T^{-1}$ ],  $C_{i,s}$  is the concentration of the source/sink fluid, and  $R_n^i$  is the  $n$ -th reaction that transforms constituent  $i$ . In the case of brine transport, the cation exchange capacity of the sand was considered negligible, such that  $R_n^i = 0$ . A linearized equation of state (3) was then used to represent density, incorporating a volumetric expansion coefficient,  $\beta_c$ , for salt concentration (4):

$$\rho = \rho_0 \exp[\beta_C(C - C_0)] \approx \rho_0 + \rho_0\beta_C(C - C_0) \quad (3)$$

$$\beta_C = \frac{1}{\rho_0} \left( \frac{\partial \rho}{\partial C} \right)_{T,P} \quad (4)$$

Solution of eqn (1) through (4) was implemented using the SEAWAT Version 4 software package, an open-source finite difference groundwater flow and transport code developed by the USGS.<sup>49</sup> SEAWAT is a modification of the MODFLOW-MT3DMS suite<sup>56,57</sup> and has been used to simulate variable density groundwater flow and transport due to transient concentration (*i.e.* salt), heat, or pressure, particularly in estuarial environments.<sup>58,59</sup> The SEAWAT simulator can track multiple constituents simultaneously, a feature that was utilized in this study to account for the influence of transient brine and NP concentrations on variable density flow behavior.

Nanoparticle transport was incorporated in the model using a balance eqn (2), with  $R_n^i$  representing the interaction between NPs and the solid surface (NP deposition and detachment). Consistent with recent laboratory and modeling investigations of NP transport in natural porous media,<sup>60</sup> NP deposition was modeled as a first-order kinetic process, where deposition is limited by a system-specific retention capacity. In the experiments conducted in this study, ionic strength was constant, so it was assumed that nMag detachment from the solid phase was negligible. Additionally, to reduce the number of model input parameters, thereby reducing non-uniqueness issues in parameter fitting, a single type of attachment site was assumed, resulting in:<sup>39</sup>

$$\sum_n R_n^i = \rho_b \frac{\partial S_i}{\partial t} = \theta_w k_{att,i} \Psi_i C_i \quad (5)$$

$$\Psi_i = \frac{S_{max,i} - S_i}{S_{max,i}} \quad (6)$$

where  $k_{att,i}$  is the attachment rate of NP constituent  $i$  [ $T^{-1}$ ],  $\rho_b$  is the bulk density of the sand [ $M L^{-3}$ ],  $S_i$  is the attached phase concentration of constituent  $i$  [ $M M^{-1}$ ],  $\Psi_i$  is the Langmuir-type blocking function for NP attachment, and  $S_{max,i}$  is the maximum retention capacity for constituent  $i$  [ $M/M$ ]. Based on traditional colloid filtration theory,<sup>26</sup> the first order attachment rate,  $k_{att,i}$  ( $T^{-1}$ ), can be represented as:

$$k_{att,i} = \frac{3(1-\theta_w)v_p}{2d_c} \alpha_i \eta_{0,i} \quad (7)$$

where  $d_c$  is the a representative collector (*i.e.*, grain) size (L). Eqn (7) was used to compute NP attachment efficiency,  $\alpha_i$ , based upon fitted values of  $k_{att,i}$  for each experiment. Details on the parameter fitting algorithm have been previously de-

scribed.<sup>61</sup> Theoretical collector efficiency,  $\eta_{0,i}$ , values were estimated with a correlation presented by Tufenkji and Elimelech:<sup>62</sup>

$$\eta_0 = 2.4A_s^{0.33} N_R^{-0.081} N_{Pe}^{-0.715} N_{vdW}^{0.052} + 0.55A_s N_R^{1.675} N_A^{0.125} + 0.22N_R^{-0.24} N_G^{1.11} N_{vdW}^{0.053} \quad (8)$$

Here,  $A_s$  is the Happel correction factor,  $N_R$  is the interception number,  $N_{Pe}$  is the Peclet number,  $N_{vdW}$  is the London-van der Waals attractive forces number,  $N_A$  is the attraction number, and  $N_G$  is the gravitational number.<sup>62</sup> The three terms in eqn (8) represent the contributions to collector efficiency by Brownian diffusion, interception, and sedimentation, respectively. The inclusion of eqn (7) and (8) in the model used in this study facilitates prediction of  $k_{att,i}$  variations with velocity for each porous medium, which is particularly important in heterogeneous domains.

Implementation of the NP transport model in the SEAWAT framework was accomplished by adapting the non-equilibrium sorption reaction module:<sup>39,42</sup>

$$R_n = \beta \left( C_i - \frac{S_i}{K_d} \right) \quad (9)$$

where  $\beta$  and  $K_d$  are specified parameters. To account for the functional dependence of  $\beta$  and  $K_d$  on NP attachment and release, as given by eqn (5) and (6), the SEAWAT simulator was modified to allow for the temporal and spatial dependence of these reaction parameters, where:

$$\beta = \theta_w k_{att}^n \psi^n \quad (10)$$

$$K_d = \frac{\theta_w k_{att}^n \psi^n}{\rho_b k_{det}^n} \quad (11)$$

The development of this model and application to 1D column transport data have previously been described,<sup>39,63</sup> but the current study demonstrates the first application of this model to predict 2.5D NP transport in a heterogeneous flow cell using parameters obtained from 1D column experiments. Longitudinal and transverse hydrodynamic dispersion values for the flow cell were estimated by model fitting to non-reactive (fluorescein + bromide) tracer tests conducted in the domain prior to nMag injection. Domain discretization and boundary conditions are described in the ESI.†

## Results & discussion

### Column results

Three column experiments were carried out to evaluate nMag mobility and to obtain model input parameters as a function of porous media type and flow rate. Experimental observations are presented in Fig. S3† as normalized effluent breakthrough curves (BTCs), plotted as a function of

dimensionless time (PVs). For both media, the nMag BTCs exhibit an asymmetrical shape and plateau at a normalized concentration of 1.0, features consistent with a retention-capacity-modified filtration process.<sup>29</sup> This behavior is also consistent with results obtained from prior studies of NP transport in porous media.<sup>19,28,29,64</sup> Slightly greater nMag mass breakthrough was observed for the coarse sand compared to the fine sand (97% vs. 92%, respectively, Table 1). The lower retention of nMag in the coarse sand column is consistent with the smaller specific surface area (SSA) of the coarse sand relative to the fine sand (SSA = 0.0125 and 0.0188 m<sup>2</sup> g<sup>-1</sup>, respectively). In contrast to previous NP transport studies that have shown reduced NP retention and increased mobility with increasing flow rate,<sup>65,66</sup> similar nMag mobility (92% versus 90% mass breakthrough) was observed for the fine grain sand at the fast (1.78 mL min<sup>-1</sup>) and slow (0.26 mL min<sup>-1</sup>) flow rates in this study, respectively.

To parameterize the NP transport simulator, the retention model represented by eqn (2), (5), and (6) was fit to each BTC to estimate the  $k_{att}$  and  $S_{max}$  parameters (Table 1), using a nonlinear least squares optimization algorithm (MATLAB, The Mathworks, Natick, MA). Incorporation of fitted attachment parameters and associated velocities and grain sizes into eqn (7) and (8) then facilitated calculation of the corresponding attachment efficiency values ( $\alpha$ ). For the two slow flow (0.26 mL min<sup>-1</sup>) column experiments, estimated attachment efficiencies were of similar magnitude, with values of  $1.7 \times 10^{-2}$  and  $4.3 \times 10^{-2}$ . This result is consistent with traditional theories for particle deposition<sup>67</sup> which assume that attachment efficiency is a function of surface and solution chemistry, independent of grain size.

Model-fitted  $S_{max}$  values increased with decreasing grain size, a trend that has been previously observed for nC<sub>60</sub> transport in different size fractions of Ottawa sand.<sup>28</sup> To incorporate the influence of variable grain size and flow rate (present in the heterogeneous flow cell) on  $S_{max}$  in the mathematical model, the approach of Li *et al.*<sup>28</sup> was employed, where  $S_{max}$  values are fit to a power function of the normalized diffusive mass flux of nMag to the surface. Fig. S4† presents a plot of parameter data and the best fit  $S_{max}$  power function (equations provided in ESI†).

### Flow field and non-reactive tracer simulations

Observations from the non-reactive tracer experiments were used in conjunction with model simulations to characterize the flow field within the heterogeneous cell and to confirm the appropriateness of the permeability values employed for the emplaced media. Based on visualization of the tracer test (fluorescein + bromide) conducted in the domain prior to nMag injection, longitudinal dispersivity was set as 0.1 cm and transverse dispersivity was set as 0.01 cm, which were the same values used by Kanel *et al.* (2008).<sup>48</sup> For the test conducted by delivering tracer in the influent chamber, qualitative comparisons of model simulations to the observed tracer front migration indicated that the simulations appro-

priately matched plume transport behavior around the lower permeability regions of the sandpack (Fig. S5†). Furthermore, quantitative comparisons of effluent concentration data to model simulations indicated that the general breakthrough and tailing shape was well-matched by the simulation results, suggesting appropriate selection of system dispersivity values (Fig. S6†). The discrepancy between the modeled and observed breakthrough times was likely due to (unquantified) variations in the background flow rate in the head-driven experimental system when the influent bottle was changed from tracer to background electrolyte.

Additional tracer tests were carried out using the two injection ports (port A4 and D4 locations shown in Fig. 1) by injecting a small pulse (190 mL) of NaBr into the background flow field. Model simulations of tracer flow paths and concentrations measured in two downstream ports (C3/C4 sampled for A4 injection and F3/F4 sampled for D4 injection) are compared in Fig. S7 and S8.† The BTCs obtained from the two sampling ports (F3 and F4) downstream of the control D4 injection were nearly identical and both reached a  $C/C_0$  value of 1.0 (Fig. S8†). For the tracer injection (A4) upstream of the fine sand lens, the BTC of downstream sampling port C3 plateaued at a  $C/C_0$  value of 1.0, while the BTC for sampling port C4 only reached  $C/C_0 = 0.78$ , likely due to the preferential flow of the tracer plume around the fine lens and the location of the sampling port C4 just below the lens (Fig. S8†). The model was able to predict the breakthrough times at the downstream ports, but the simulated  $C/C_0$  plateau maximum values differed slightly compared to the observed values for ports F3 and C4. The simulated  $C/C_0$  maximum was slightly lower than the observed value in F3 (downstream from the control injection) and higher than the observed value for C4 (downstream from the fine sand lens injection). These differences can be attributed to the relative positions of the sampling ports and the extent of the tracer plume spread (F3 located on the edge of the tracer plume and C4 directly below the fine sand lens, Fig. S7†), where concentration values would vary greatly over a small (*i.e.*, mm-scale) distance. Despite the discrepancies in breakthrough plateaus, the timing and shapes of the port tracer breakthrough curves were generally well-matched, providing confirmation of the model permeability and dispersivity values.

### Nanoparticle transport in flow cells

To investigate the transport of nMag in a heterogeneous system, two NP injections were performed; the first in the background coarse sand, and the second immediately upgradient from a lens of lower permeability media (fine sand). Fig. 2 presents the flow path of the NP plume injected upstream of a fine sand lens, while images of the background control injection (no lens) are presented in Fig. S9.† The retained nMag can be seen as a light brown shade, while the mobile NP pulse appears as a darker, reddish-brown color. The nMag pulse preferentially flowed around the lower permeability fine sand lens, but eventually penetrated into the lens. The

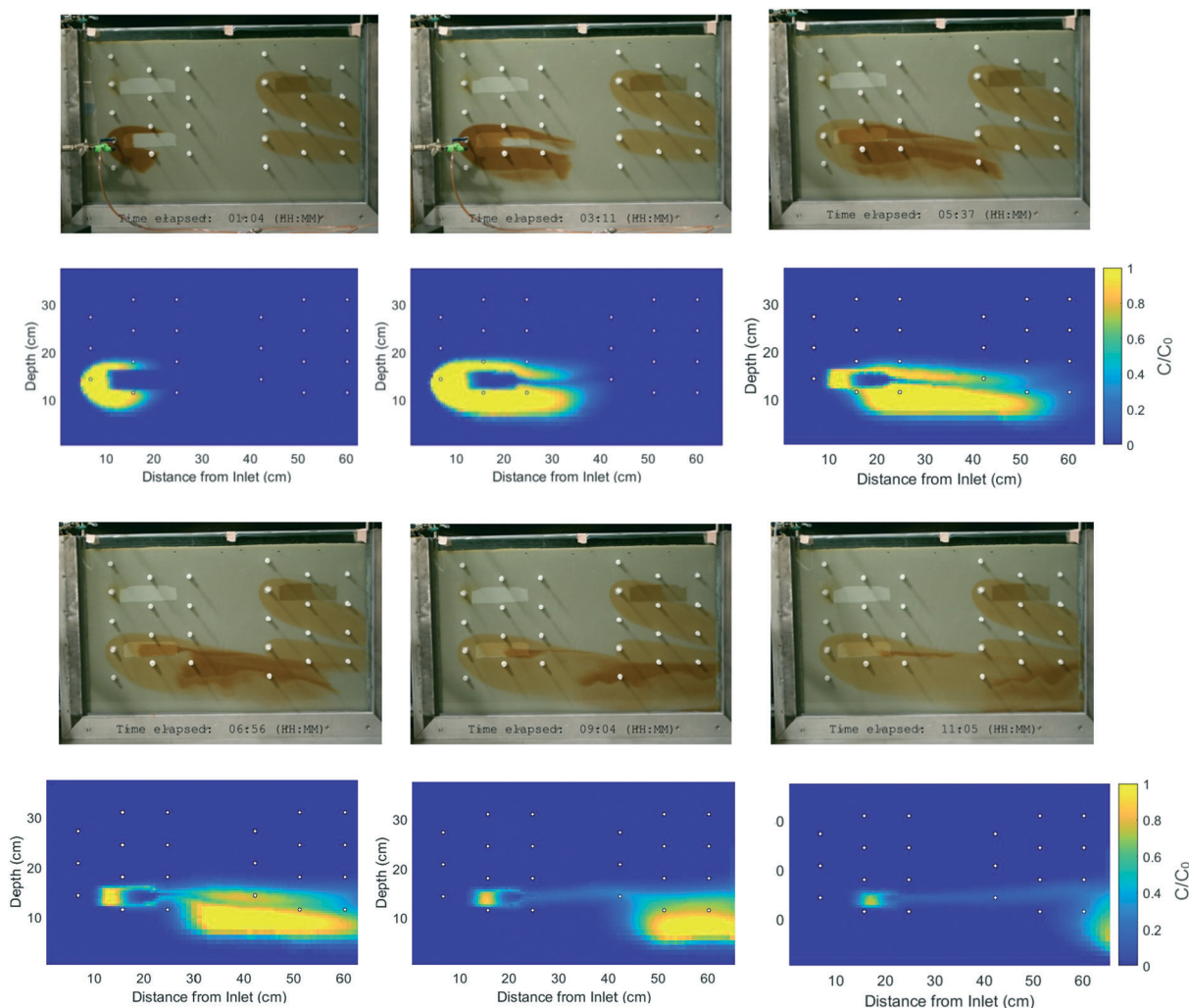


Fig. 2 Observed and predicted nMag transport through 80–100 mesh Ottawa sand lens. Time elapsed since start of injection is shown in hours: minutes.

downward sloping nMag flow path observed in both injections was due to the higher density of the NP suspension compared to that of brine alone (*i.e.*,  $1.07 \text{ g mL}^{-1}$  versus  $1.06 \text{ g mL}^{-1}$ , respectively). Kanel *et al.* observed a similar downward migration of zero-valent iron NPs in a two-dimensional transport study, but in that case the effect was more pronounced due to a density contrast of  $0.036 \text{ g mL}^{-1}$  between the background electrolyte solution and NP suspension.<sup>48</sup>

A wave-like flow pattern was observed at the bottom of the NP plume (Fig. 2), which is indicative of interface instability created by the denser nMag suspension flowing above the less dense brine solution.<sup>68</sup> This perturbation of the injected pulse results in dilute and concentrated regions of the nMag plume, which can be identified by the different shades of brown observed in Fig. 2 and S9†. These observations indicate that even slight fluid density contrasts (*i.e.*,  $0.01 \text{ g mL}^{-1}$ ) can impact the transport of NP suspensions in a 2.5D system. The potential influence of such contrasts in a larger scale, subsurface injection scenario would likely depend upon the degree of horizontal anisotropy of the formation.<sup>69</sup> (The labo-

ratory flow cell used in the current study was locally isotropic).

Using the  $k_{\text{att}}$  and  $S_{\text{max}}$  values obtained from parameterization of the column results (Table 1), model simulations of the nMag flow cell injection experiments were conducted. The predicted nMag flow paths were consistent with the observed transport (Fig. 2 and S9†). The model was able to capture some of the interface instability (wave-like pattern) at the bottom of the nMag pulse injected upstream of the fine sand lens. In addition to these visual comparisons, Fig. 3 and S10† present comparisons between model simulations and measured BTCs in side-ports downgradient of the injection ports. The simulated BTCs for the control injection exhibited close agreement with the measured pulse breakthrough in downstream ports E4 and F4 (very little breakthrough observed for ports E3 and F3). However, the experimental BTCs exhibited a downward sloping trend that was not captured by the simulation, which can be attributed to the development of interface instability (due to density differences between the nanoparticle suspension and background brine solution)

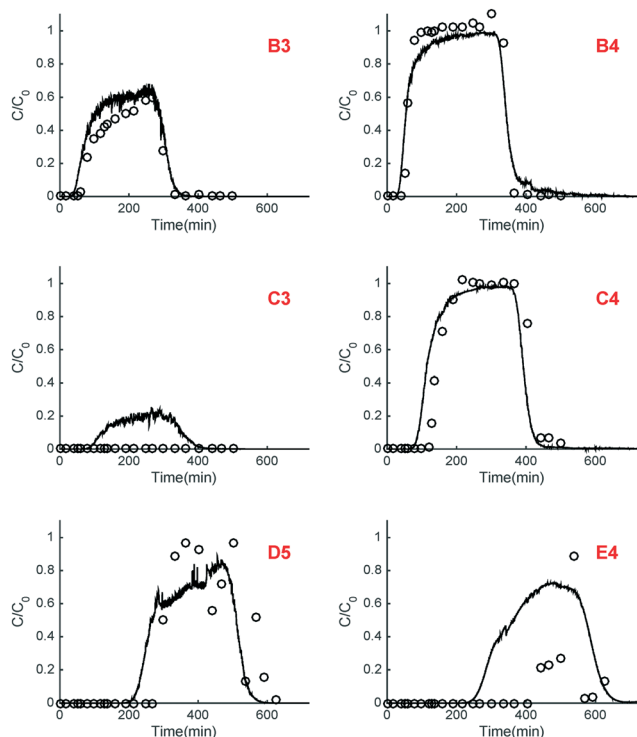


Fig. 3 Measured (open circles) compared to predicted (solid line) nMag effluent concentrations for fine sand (80–100 mesh Ottawa sand) lens injection. Port location is noted in top right of each figure.

that resulted in a lower concentration region passing by the sampling ports (Fig. S9 and S10<sup>†</sup>).

The effect of interface instability on nMag transport was also observed in the port measurements collected during the fine grain sand lens injection (Fig. 3), which exhibited a wave-like front that increased in amplitude as the pulse traveled downstream (*i.e.*, compare measurements in ports B3 and B4, with those downstream, D5 and E4). Model simulations captured the passing of these wave-like structures in the D5 and E4 port concentrations (Fig. 3), but did not adequately describe the magnitude of this behavior. These instabilities are highly sensitive to both the relative densities of the two fluids and random variations in permeability within the system, characteristics which are difficult to accurately represent in the numerical model.<sup>25</sup> Thus, the discrepancies between the model results and the observed behavior can be attributed to fine scale variations in the coarse sand permeability which cannot be accurately resolved by the model.

To further explore the role of density in NP transport, a sensitivity analysis was performed to examine the response of nMag transport to changes in the density contrast (0.0, 0.01 g mL<sup>-1</sup>, and 0.02 g mL<sup>-1</sup>) relative to the background solution (brine,  $\rho = 1.06$  g mL<sup>-1</sup>), shown in Fig. S11.<sup>†</sup> The simulations considered both NP transport and solid-phase attachment. The density contrast of 0 g mL<sup>-1</sup> was simulated by neglecting the influence of nMag concentration on injection fluid density. With increasing density contrast between the injected plume and the background solution, the downward sloping

flow and interface instabilities increased (Fig. S11<sup>†</sup>). At a density contrast of 0.01 g mL<sup>-1</sup> (the density difference between 2500 mg L<sup>-1</sup> nMag and brine in this study), the plume migrated vertically approximately 1.5 cm over a lateral distance of 20 cm. For a density contrast of 0.02 g mL<sup>-1</sup>, this vertical migration was 2.75 cm over the 20 cm horizontal distance. The ability to predict the influence of contrast agent concentrations on NP transport can assist in the design and implementation of field-scale applications. Furthermore, these results suggest that compositional density effects should be considered in systems where even minimal density differences are anticipated.

### Nanoparticle retention

At the completion of the flow cell experiment, the system was disassembled and solid phase samples were collected from several regions of the flow cell to quantify the distribution of retained nMag. Fig. 4 shows a comparison of the measured and simulated nMag retention within the flow cell. The average nMag retention values in the coarse sand background and fine sand lens,  $83 \pm 27$  and  $94 \pm 32$   $\mu\text{g Fe}_3\text{O}_4 \text{ g}^{-1}$  media (Fig. 4b), respectively, compare favorably with the column-measured  $S_{\text{max}}$  values of 67 and 124  $\mu\text{g Fe}_3\text{O}_4 \text{ g}^{-1}$  media, respectively (Table 1). The highest nMag retention was measured in the regions immediately downstream of the injection ports, in the upgradient portion of the fine sand lens, and immediately below the upgradient section of the fine sand lens (Fig. 4b). Fig. 4d presents percent error deviations between predicted and measured nMag retention. Inspection of the figure reveals that model simulations are generally consistent with the measured retention values in the background coarse sand and in the upgradient region of the fine sand lens. However, higher retention was predicted in the downgradient region of the fine sand lens compared to measured values, and also directly upgradient of the injection port. Despite these inconsistencies, the model was able to capture the observed retention trends and retained mass to within approximately 0.2 orders of magnitude.

To further explore nMag retention, SEM images of coarse and fine sand samples collected from the retained plume regions are shown in Fig. S12.<sup>†</sup> Images of background sand that was not in contact with nMag are also shown for comparison purposes. Using an EDS detector on the SEM and the spectrum function, elevated iron concentrations were observed in regions of attached NPs compared to NP-free sand (*e.g.*, 2.4 wt% vs. 0.75 wt% Fe, respectively, shown in Fig. S13<sup>†</sup>).

## Conclusions

Assessment of the potential performance of engineered NPs for a range of proposed subsurface applications requires the ability to predict NP mobility through porous media in the environment. The coupled experimental measurements and mathematical modeling studies presented here demonstrate the transport behavior of nMag in a 2.5D heterogeneous flow

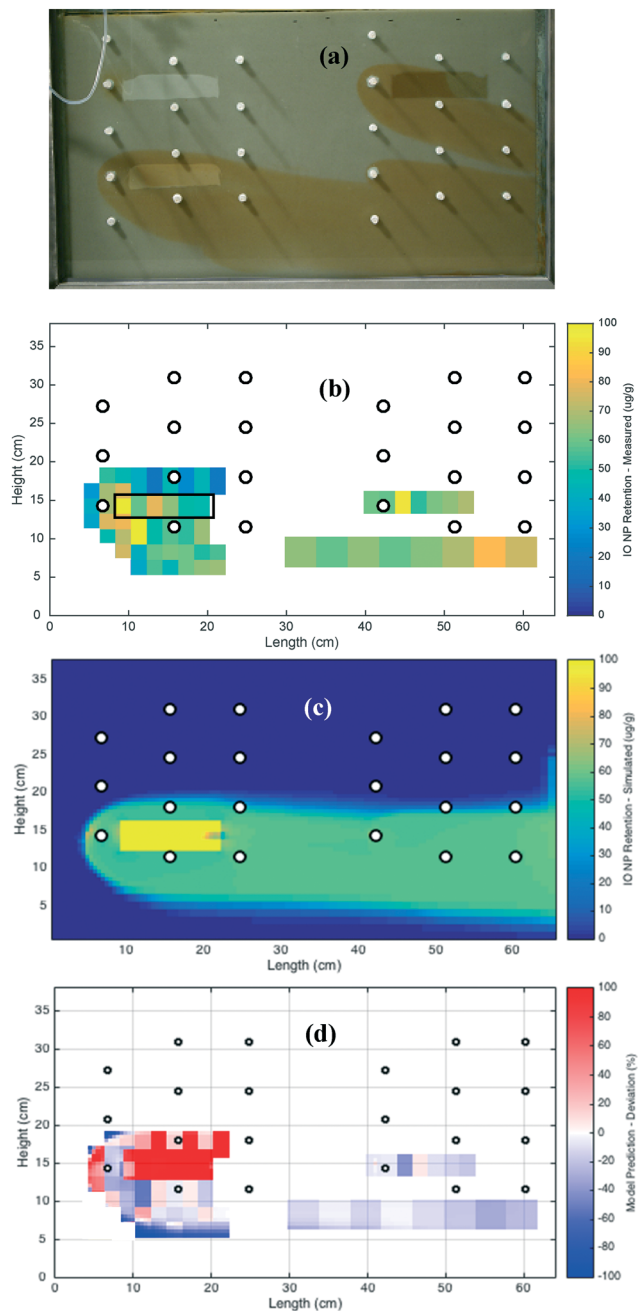


**Fig. 4** (a) Observed, (b) measured, (c) simulated, and (d) model simulation percent error (*i.e.*  $100 \times ([\text{simulated retention}] - [\text{measured retention}]) / [\text{measured retention}]$ ) of nMag retention following flow cell experiment. Average measured nMag retention for fine sand lens ( $94 \pm 32$ ) was calculated from concentrations measured inside lens, average measured retention for coarse sand ( $83 \pm 27$ ) was calculated using all other measured values shown in Fig. 4b.

cell. An advanced polymer coating technique yielded stable and mobile nMag suspensions under high salinity conditions (2 wt%  $\text{CaCl}_2$ , 8 wt%  $\text{NaCl}$ ), which is essential for the successful deployment of NPs. A multi-dimensional NP transport model that accounts for attachment kinetics and the influence of varying electrolyte and NP concentrations on flow density accurately reproduced the migration of the nMag

pulse, aqueous phase concentrations measured from sampling ports, and solid-phase (retained NP) concentrations. The presence of a lens containing lower permeability porous media resulted in preferential flow around the lens initially, but eventually the nMag plume penetrated the lens, which slowed down the plume migration and led to a prolonged release of nMag from the lens, demonstrating the importance of porous media heterogeneity on NP transport.

Although previous studies have explored the implications of NP transport in a field-scale scenario using parameters determined from column experiments, this work provides the first direct comparison of parameterized model simulations to spatially distributed experimental measurements of NP transport and retention in a heterogeneous, 2.5D domain. Experimental observations and model simulations demonstrated that fluid density contrasts (*e.g.*,  $0.01 \text{ g mL}^{-1}$ ) can play an important role in the mobility of NP suspensions in heterogeneous porous media, and therefore, should be accounted for when attempting to simulate or predict NP transport in subsurface environments. While this study focused on magnetite, the NP transport model can be applied to a range of environmental conditions, including NP delivery scenarios in salinity-impacted aquifer formations.

## Acknowledgements

This work was supported by the Advanced Energy Consortium (<http://www.beg.utexas.edu/aec/>) Project #BEG-13-01. Member companies include Repsol, Shell, and Total. SEM imaging was performed at the Harvard University Center for Nanoscale Systems (CNS), a member of the National Nanotechnology Infrastructure Network (NNIN), which is sponsored by the National Science Foundation under Award no. ECS-0335765.

## References

- 1 Y. Liu, S. A. Majetich, R. D. Tilton, D. S. Sholl and G. V. Lowry, TCE Dechlorination Rates, Pathways, and Efficiency of Nanoscale Iron Particles with Different Properties, *Environ. Sci. Technol.*, 2005, 39(5), 1338–1345.
- 2 J. Quinn, C. Geiger, C. Clausen, K. Brooks, C. Coon, S. O'Hara, T. Krug, D. Major, W.-S. Yoon, A. Gavaskar and T. Holdsworth, Field Demonstration of DNAPL Dehalogenation Using Emulsified Zero-Valent Iron, *Environ. Sci. Technol.*, 2005, 39(5), 1309–1318.
- 3 D. O'Carroll, B. Sleep, M. Krol, H. Boparai and C. Kocur, Nanoscale zero valent iron and bimetallic particles for contaminated site remediation, *Adv. Water Resour.*, 2013, 51, 104–122.
- 4 N. Saleh, T. Phenrat, K. Sirk, B. Dufour, J. Ok, T. Sarbu, K. Matyjaszewski, R. D. Tilton and G. V. Lowry, Adsorbed Triblock Copolymers Deliver Reactive Iron Nanoparticles to the Oil/Water Interface, *Nano Lett.*, 2005, 5(12), 2489–2494.
- 5 J.-F. Liu, Z.-S. Zhao and G.-B. Jiang, Coating  $\text{Fe}_3\text{O}_4$  Magnetic Nanoparticles with Humic Acid for High Efficient Removal

- of Heavy Metals in Water, *Environ. Sci. Technol.*, 2008, 42(18), 6949–6954.
- 6 W. Tungittiplakorn, L. W. Lion, C. Cohen and J.-Y. Kim, Engineered Polymeric Nanoparticles for Soil Remediation, *Environ. Sci. Technol.*, 2004, 38(5), 1605–1610.
  - 7 S. Ryoo, A. R. Rahmani, K. Y. Yoon, M. Prodanović, C. Kotsmar, T. E. Milner, K. P. Johnston, S. L. Bryant and C. Huh, Theoretical and experimental investigation of the motion of multiphase fluids containing paramagnetic nanoparticles in porous media, *J. Pet. Sci. Eng.*, 2012, 81, 129–144.
  - 8 C. Kotsmar, K. Y. Yoon, H. Yu, S. Y. Ryoo, J. Barth, S. Shao, M. Prodanović, T. E. Milner, S. L. Bryant, C. Huh and K. P. Johnston, Stable Citrate-Coated Iron Oxide Superparamagnetic Nanoclusters at High Salinity, *Ind. Eng. Chem. Res.*, 2010, 49(24), 12435–12443.
  - 9 A. R. Rahmani, A. E. Athey, J. Chen and M. J. Wilt, Sensitivity of dipole magnetic tomography to magnetic nanoparticle injectates, *J. Appl. Geophys.*, 2014, 103, 199–214.
  - 10 A. R. Petosa, D. P. Jaisi, I. R. Quevedo, M. Elimelech and N. Tufenkji, Aggregation and deposition of engineered nanomaterials in aquatic environments: Role of physicochemical interactions, *Environ. Sci. Technol.*, 2010, 44(17), 6532–6549.
  - 11 F. He, M. Zhang, T. Qian and D. Zhao, Transport of carboxymethyl cellulose stabilized iron nanoparticles in porous media: Column experiments and modeling, *J. Colloid Interface Sci.*, 2009, 334, 96–102.
  - 12 T. Phenrat, A. Cihan, H.-J. Kim, M. Mital, T. Illangasekare and G. V. Lowry, Transport and Deposition of Polymer-Modified Fe<sub>0</sub> Nanoparticles in 2-D Heterogeneous Porous Media: Effects of Particle Concentration, Fe<sub>0</sub> Content, and Coatings, *Environ. Sci. Technol.*, 2010, 44(23), 9086–9093.
  - 13 P. C. Hiemenz and R. Rajagopalan, *Principles of Colloid and Surface Chemistry*, Marcel Dekker, Inc., New York, NY, 3rd edn, 1997.
  - 14 N. Saleh, H.-J. Kim, T. Phenrat, K. Matyjaszewski, R. D. Tilton and G. V. Lowry, Ionic Strength and Composition Affect the Mobility of Surface-Modified Fe<sub>0</sub> Nanoparticles in Water-Saturated Sand Columns, *Environ. Sci. Technol.*, 2008, 42(9), 3349–3355.
  - 15 T. Ben-Moshe, I. Dror and B. Berkowitz, Transport of metal oxide nanoparticles in saturated porous media, *Chemosphere*, 2010, 81(3), 387–393.
  - 16 R. Kretzschmar and H. Sticher, Transport of Humic-Coated Iron Oxide Colloids in a Sandy Soil: Influence of Ca<sup>2+</sup> and Trace Metals, *Environ. Sci. Technol.*, 1997, 31(12), 3497–3504.
  - 17 B. Espinasse, E. M. Hotze and M. R. Wiesner, Transport and Retention of Colloidal Aggregates of C<sub>60</sub> in Porous Media: Effects of Organic Macromolecules, Ionic Composition, and Preparation Method, *Environ. Sci. Technol.*, 2007, 41(21), 7396–7402.
  - 18 D. P. Jaisi, N. B. Saleh, R. E. Blake and M. Elimelech, Transport of Single-Walled Carbon Nanotubes in Porous Media: Filtration Mechanisms and Reversibility, *Environ. Sci. Technol.*, 2008, 42(22), 8317–8323.
  - 19 Y. Liang, S. A. Bradford, J. Simunek, H. Vereecken and E. Klumpp, Sensitivity of the transport and retention of stabilized silver nanoparticles to physicochemical factors, *Water Res.*, 2013, 47(7), 2572–2582.
  - 20 J. Jiang, G. Oberdörster and P. Biswas, Characterization of size, surface charge, and agglomeration state of nanoparticle dispersions for toxicological studies, *J. Nanopart. Res.*, 2009, 11(1), 77–89.
  - 21 Y. Wang, H. Zhu, M. D. Becker, J. Englehart, L. M. Abriola, V. L. Colvin and K. D. Pennell, Effect of Surface Coating Composition on Quantum Dot Mobility in Porous Media, *J. Nanopart. Res.*, 2013, 15(8), 1805.
  - 22 H. G. Bagaria, Z. Xue, B. M. Neilson, A. J. Worthen, K. Y. Yoon, S. Nayak, V. Cheng, J. H. Lee, C. W. Bielawski and K. P. Johnston, Iron Oxide Nanoparticles Grafted with Sulfonated Copolymers are Stable in Concentrated Brine at Elevated Temperatures and Weakly Adsorb on Silica, *ACS Appl. Mater. Interfaces*, 2013, 5(8), 3329–3339.
  - 23 Z. Xue, E. Foster, Y. Wang, S. Nayak, V. Cheng, V. W. Ngo, K. D. Pennell, C. W. Bielawski and K. P. Johnston, Effect of Grafted Copolymer Composition on Iron Oxide Nanoparticle Stability and Transport in Porous Media at High Salinity, *Energy Fuels*, 2014, 28(6), 3655–3665.
  - 24 E. E. Ureña-Benavides, E. L. Lin, E. L. Foster, Z. Xue, M. Ortiz, Y. Fei, E. S. Larsen, A. A. Kmetz, B. A. Lyon, C. W. Bielawski, K. D. Pennell, C. J. Ellison and K. P. Johnston, Low Adsorption of Magnetite Nanoparticles with Uniform Polyelectrolyte Coatings in Concentrated Brine on Model Silica and Sandstone, *Ind. Eng. Chem. Res.*, 2016, 55(6), 1522–1532.
  - 25 C. T. Simmons, T. R. Fenstemaker and J. M. Sharp Jr, Variable-density groundwater flow and solute transport in heterogeneous porous media: approaches, resolutions and future challenges, *J. Contam. Hydrol.*, 2001, 52(1–4), 245–275.
  - 26 K. Yao, M. T. Habibian and C. R. O'Melia, Water and Waste Water Filtration: Concepts and Applications, *Environ. Sci. Technol.*, 1971, 5(11), 1105–1112.
  - 27 N. Tufenkji and M. Elimelech, Breakdown of colloid filtration theory: Role of the secondary energy minimum and surface charge heterogeneities, *Langmuir*, 2005, 21(3), 841–852.
  - 28 Y. Li, Y. Wang, K. D. Pennell and L. M. Abriola, Investigation of the Transport and Deposition of Fullerene (C<sub>60</sub>) Nanoparticles in Quartz Sands under Varying Flow Conditions, *Environ. Sci. Technol.*, 2008, 42(19), 7174–7180.
  - 29 Y. Wang, Y. Li, J. Fortner, J. B. Hughes, L. M. Abriola and K. D. Pennell, Transport and Retention of Nanoscale C<sub>60</sub> Aggregates in Water-Saturated Porous Media, *Environ. Sci. Technol.*, 2008, 42(10), 3588–3594.
  - 30 X. Li, T. D. Scheibe and W. P. Johnson, Apparent Decreases in Colloid Deposition Rate Coefficients with Distance of Transport under Unfavorable Deposition Conditions: A General Phenomenon, *Environ. Sci. Technol.*, 2004, 38(21), 5616–5625.

- 31 S. Xu, B. Gao and J. E. Saiers, Straining of colloidal particles in saturated porous media, *Water Resour. Res.*, 2006, **42**(12), W12S16.
- 32 S. A. Bradford, S. R. Yates, M. Bettahar and J. Simunek, Physical factors affecting the transport and fate of colloids in saturated porous media, *Water Resour. Res.*, 2002, **38**(12), 63.
- 33 Y. Hong, R. J. Honda, N. V. Myung and S. L. Walker, Transport of iron-based nanoparticles: Role of magnetic properties, *Environ. Sci. Technol.*, 2009, **43**(23), 8834–8839.
- 34 T. Raychoudhury, N. Tufenkji and S. Ghoshal, Straining of polyelectrolyte-stabilized nanoscale zero valent iron particles during transport through granular porous media, *Water Res.*, 2014, **50**, 80–89.
- 35 J. Englehart, B. A. Lyon, M. D. Becker, Y. Wang, L. M. Abriola and K. D. Pennell, Influence of a polymer sunscreen additive on the transport and retention of titanium dioxide nanoparticles in water-saturated porous media, *Environ. Sci.: Nano*, 2015, **3**, 157–168.
- 36 A. M. El Badawy, A. Aly Hassan, K. G. Scheckel, M. T. Suidan and T. M. Tolaymat, Key Factors Controlling the Transport of Silver Nanoparticles in Porous Media, *Environ. Sci. Technol.*, 2013, **47**(9), 4039–4045.
- 37 Z. Li, E. Sahle-Demessie, A. A. Hassan and G. A. Sorial, Transport and deposition of CeO<sub>2</sub> nanoparticles in water-saturated porous media, *Water Res.*, 2011, **45**(15), 4409–4418.
- 38 X. Liu, D. M. O'Carroll, E. J. Petersen, Q. Huang and C. L. Anderson, Mobility of Multiwalled Carbon Nanotubes in Porous Media, *Environ. Sci. Technol.*, 2009, **43**(21), 8153–8158.
- 39 M. D. Becker, Y. Wang, J. L. Paulsen, Y. Q. Song, L. M. Abriola and K. D. Pennell, In situ Measurement and Simulation of Nano-Magnetite Mobility in Porous Media Subject to Transient Salinity, *Nanoscale*, 2015, **7**(3), 1047–1057.
- 40 S. A. Bradford, S. Torkzaban, H. Kim and J. Simunek, Modeling Colloid and Microorganism Transport and Release with Transients in Solution Ionic Strength, *Water Resour. Res.*, 2012, **48**(9), W09509.
- 41 T. Tosco, A. Tiraferri and R. Sethi, Ionic Strength Dependent Transport of Microparticles in Saturated Porous Media: Modeling Mobilization and Immobilization Phenomena under Transient Chemical Conditions, *Environ. Sci. Technol.*, 2009, **43**(12), 4425–4431.
- 42 C. Bai and Y. Li, Modeling the Transport and Retention of nC<sub>60</sub> Nanoparticles in the Subsurface under Different Release Scenarios, *J. Contam. Hydrol.*, 2012, **136**–137, 43–55.
- 43 E. Cullen, D. M. O'Carroll, E. K. Yanful and B. Sleep, Simulation of the subsurface mobility of carbon nanoparticles at the field scale, *Adv. Water Resour.*, 2010, **33**, 361–371.
- 44 C. Bai and Y. Li, Time series analysis of contaminant transport in the subsurface: Applications to conservative tracer and engineered nanomaterials, *J. Contam. Hydrol.*, 2014, **164**, 153–162.
- 45 J. Li, S. R. C. Rajajayavel and S. Ghoshal, Transport of carboxymethyl cellulose-coated zerovalent iron nanoparticles in a sand tank: Effects of sand grain size, nanoparticle concentration and injection velocity, *Chemosphere*, 2016, **150**, 8–16.
- 46 C. M. Kocur, A. I. Chowdhury, N. Sakulchaicharoen, H. K. Boparai, K. P. Weber, P. Sharma, M. M. Krol, L. Austrins, C. Peace, B. E. Sleep and D. M. O'Carroll, Characterization of nZVI Mobility in a Field Scale Test, *Environ. Sci. Technol.*, 2014, **48**(5), 2862–2869.
- 47 R. L. Johnson, J. T. Nurmi, G. S. O'Brien Johnson, D. Fan, R. L. O'Brien Johnson, Z. Shi, A. J. Salter-Blanc, P. G. Tratnyek and G. V. Lowry, Field-Scale Transport and Transformation of Carboxymethylcellulose-Stabilized Nano Zero-Valent Iron, *Environ. Sci. Technol.*, 2013, **47**(3), 1573–1580.
- 48 S. R. Kanel, R. R. Goswami, T. P. Clement, M. O. Barnett and D. Zhao, Two Dimensional Transport Characteristics of Surface Stabilized Zero-valent Iron Nanoparticles in Porous Media, *Environ. Sci. Technol.*, 2008, **42**(3), 896–900.
- 49 C. D. Langevin, D. T. Thorne Jr., A. M. Dausman, M. C. Sukop and W. Guo, *SEAWAT Version 4: A Computer Program for Simulation of Multi-Species Solute and Heat Transport*, U. S. Geological Survey, Reston, Virginia, 2008, p. 48.
- 50 P. Babakhani, F. Fagerlund, A. Shamsai, G. V. Lowry and T. Phenrat, Modified MODFLOW-based model for simulating the agglomeration and transport of polymer-modified Fe<sup>0</sup> nanoparticles in saturated porous media, *Environ. Sci. Pollut. Res.*, 2015, 1–20.
- 51 M. M. Krol, A. J. Oleniuk, C. M. Kocur, B. E. Sleep, P. Bennett, Z. Xiong and D. M. O'Carroll, A Field-Validated Model for In Situ Transport of Polymer-Stabilized nZVI and Implications for Subsurface Injection, *Environ. Sci. Technol.*, 2013, **47**(13), 7332–7340.
- 52 S. Kralj, D. Makovec, S. Čampelj and M. Drogenik, Producing ultra-thin silica coatings on iron-oxide nanoparticles to improve their surface reactivity, *J. Magn. Magn. Mater.*, 2010, **322**(13), 1847–1853.
- 53 M. Elimelech, M. Nagai, C.-H. Ko and J. N. Ryan, Relative insignificance of mineral grain zeta potential to colloid transport in geochemically heterogeneous porous media, *Environ. Sci. Technol.*, 2000, **34**(11), 2143–2148.
- 54 ASTM, *Standard Test Method for Permeability of Granular Soils (Constant Head)*. In *ASTM D2434–68*, ASTM International, West Conshohocken, PA, 2006, p. 5.
- 55 M. R. Giles, Mass Transfer and Problems of Secondary Porosity Creation in Deeply Buried Hydrocarbon Reservoirs, *Mar. Pet. Geol.*, 1987, **4**, 188–204.
- 56 C. Zheng and P. P. Wang, *MT3DMS: A Modular Three-Dimensional Multispecies Transport Model for Simulation of Advection, Dispersion, and Chemical Reactions of Contaminants in Groundwater Systems; Documentation and User's Guide*. In 1999, p. 220.
- 57 A. W. Harbaugh, E. R. Banta, M. C. Hill and M. G. McDonald, *MODFLOW-2000, The U.S. Geological Survey Modular Ground-Water Model – User guide to modularization*

- concepts and the ground-water flow process*, U.S. Geological Survey, 2000, p. 130.
- 58 D. Thorne, C. D. Langevin and M. C. Sukop, Addition of Simultaneous Heat and Solute Transport and Variable Fluid Viscosity to SEAWAT, *Comput. Geosci.*, 2006, 32, 1758–1768.
- 59 R. R. Goswami and T. P. Clement, Laboratory-Scale Investigation of Saltwater Intrusion Dynamics, *Water Resour. Res.*, 2007, 43(4), W04418.
- 60 E. Goldberg, M. Scheringer, T. D. Bucheli and K. Hungerbühler, Critical Assessment of Models for Transport of Engineered Nanoparticles in Saturated Porous Media, *Environ. Sci. Technol.*, 2014, 48(21), 12732–12741.
- 61 M. D. Becker, Y. Wang, K. D. Pennell and L. M. Abriola, A Multi-Constituent Site Blocking Model for Nanoparticle and Stabilizing Agent Transport in Porous Media, *Environ. Sci.: Nano*, 2015, 2, 155–166.
- 62 N. Tufenkji and M. Elimelech, Correlation Equation for Predicting Single-Collector Efficiency in Physicochemical Filtration in Saturated Porous Media, *Environ. Sci. Technol.*, 2004, 38(2), 529–536.
- 63 M. D. Becker, On the Influence of Co-Constituents on Nanoparticle Transport in Heterogeneous Porous Media, *PhD Dissertation*, Tufts University, 2015.
- 64 S. A. Bradford, S. Torkzaban and J. Simunek, Modeling colloid transport and retention in saturated porous media under unfavorable attachment conditions, *Water Resour. Res.*, 2011, 47(10), 1–12.
- 65 C. Ko and M. Elimelech, The “Shadow Effect” in Colloid Transport and Deposition Dynamics in Granular Porous Media: Measurements and Mechanisms, *Environ. Sci. Technol.*, 2000, 34(17), 3681–3689.
- 66 E. Pazmino, J. Trauscht, B. Dame and W. P. Johnson, Power Law Size-Distributed Heterogeneity Explains Colloid Retention on Soda Lime Glass in the Presence of Energy Barriers, *Langmuir*, 2014, 30(19), 5412–5421.
- 67 M. Elimelech, X. Jia, J. Gregory and R. Williams, *Particle Deposition & Aggregation: Measurement, Modelling and Simulation*, Butterworth-Heinemann, Woburn, MA, 1998.
- 68 R. A. Schincariol and F. W. Schwartz, An experimental investigation of variable density flow and mixing in homogeneous and heterogeneous media, *Water Resour. Res.*, 1990, 26(10), 2317–2329.
- 69 A. Salama, A. Negara, M. El Amin and S. Sun, Numerical investigation of nanoparticles transport in anisotropic porous media, *J. Contam. Hydrol.*, 2015, 181, 114–130.